Correspondence to:
M. Hu,
mmhu@hku.hk

Coefficients of Reaction-Diffusion Processes Derived From Patterns in Rocks

Chong Liu[1,2] , Victor M. Calo[3], Klaus Regenauer-Lieb[2,4], and Manman Hu[1]

[1]Department of Civil Engineering, The University of Hong Kong, Hong Kong, China, [2]WA School of Mines: Minerals, Energy and Chemical Engineering, Curtin University, Bentley, WA, Australia, [3]School of Electrical Engineering, Computing and Mathematical Sciences, Curtin University, Perth, WA, Australia, [4]School of Minerals and Energy Resources Engineering, UNSW, Sydney, NSW, Australia

Abstract Self-organizing diffusion-reaction systems naturally form complex patterns under far-from-equilibrium conditions. A representative example is the rhythmic concentration pattern of Fe-oxides in Zebra rocks; these patterns include reddish-brown stripes, rounded rods, and elliptical spots. Similar patterns are observed in the banded iron formations, which are presumed to have formed in the early earth under global glaciation. We propose that such patterns can be used directly (e.g., by computer-vision-analysis) to infer basic quantities relevant to their formation giving information on generalized chemical gradients. Here we present a phase-field model that quantitatively captures the distinct Zebra rock patterns based on the concept of phase separation that describes the process forming Liesegang stripes. We find that diffusion coefficients (the bulk self-diffusivities of the native species and the mobility of the reaction product) play an essential role in controlling the appearance of regular stripe patterns as well as the transition from stripes to spots. The numerical results are carefully benchmarked with well-established empirical spacing law, width law, timing law and the Matalon-Packter law. Using this model, we invert for the important process parameters originating from the intrinsic material properties, the self-diffusivity ratio and the mobility of Fe-oxides with a series of Zebra rock samples. This study allows a quantitative prediction of the generalized chemical gradients in mineralized source rocks without intrusive measurements, providing a better intuition for the mineral exploration space.

Plain Language Summary Patterns in nature are observed in disparate fields of science in biology, geology, mechanics, atmospheric physics, chemistry and others. A unifying principle to decipher those patterns is using a reaction-diffusion approach, as employed here, when implemented in numerical simulations, can deliver a perfect match to patterns observed in nature. Here we go one step further and show that dynamic coefficients describing the concentrations and mobility of valuable species such as iron oxide can be derived from the images. The proposed algorithms are benchmarked on the Zebra banded rock in Western Australia. The broader impact of the presented work includes the development of a future exploration tool based on computer-version, revealing high grades of iron in the prominent worldwide banded iron formations which bear similar characteristic stripes. Using a physics-based model, our formulation also captures the interesting phenomenon of transition from bands to spots that has not been addressed before.
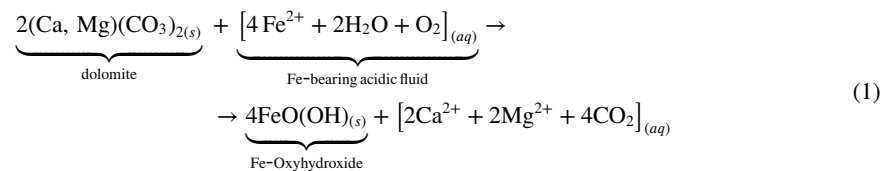
1. Introduction

Self-organization develops autonomously in reaction-diffusion systems and is observed in many rock textures in geology (Abrajevitch et al., 2018; Al-Ghoul & Sultan, 2019; Kelka et al., 2017; May et al., 2019; Msharrafieh et al., 2016; Regenauer-Lieb et al., 2021; Wang et al., 2015). In general, two necessary conditions are required to induce self-organization: (a) the governing Thermal, Hydrological, Mechanical, Chemical, Electrical (THMCE) reactions and diffusion processes are far from the equilibrium; and (b) at least two processes actively interact in the reaction-diffusion system.

Herein, we present a study on the hypothesis that these patterns can be used to derive the diffusion coefficients of their underlying reaction-diffusion equation. We thus aim to develop a robust computational platform for new image inversion techniques without intrusive interaction to the investigated rock mass. The platform is built for the future inclusion of computer vision algorithms providing image data sets from, for example, drone flights or airborne photography, thus enabling new physics-based quantitative exploration techniques.

The specific self-organizing system considered in this study is the Zebra Rock pattern in the north of Western Australia which shows the rhythmic concentration of Fe-oxides (hematite) as seen in many sedimentary rocks worldwide (Wang et al., 2015). No other banding pattern is as distinct as Zebra rock. This is argued to be related to the primary texture of the original rock, consisting of very fine-grained and well-sorted quartz in which the porosity is very small (Kawahara et al., 2022). The Zebra rock formation is, therefore, an ideal analogue of many pattern-forming processes related to subsurface mass movements. A model that combines both field observations and theoretical modeling involving fluid chemistry and fluid flow in porous media has been suggested to explain similar patterns found in Utah, and Arizona (Wang et al., 2015). The mineral hematite is a late-stage transformation product of Fe-Oxyhydroxide which has been identified in the case of the Zebra rock as the precipitate of the ferrous ions in an acidic geothermal environment according to the following chemical reaction (Kawahara et al., 2022)

$$\underbrace{2(\text{Ca, Mg})(\text{CO}_3)_{2(s)}}_{\text{dolomite}} + \underbrace{\left[4\,\text{Fe}^{2+} + 2\text{H}_2\text{O} + \text{O}_2\right]_{(aq)}}_{\text{Fe−bearing acidic fluid}} \rightarrow$$
$$\rightarrow \underbrace{4\text{FeO(OH)}_{(s)}}_{\text{Fe−Oxyhydroxide}} + \left[2\text{Ca}^{2+} + 2\text{Mg}^{2+} + 4\text{CO}_2\right]_{(aq)} \quad (1)$$

The chemical analysis by Retallack (2021) suggests low CaO and MgO content in the Zebra rocks, for which Kawahara et al. (2022) explain that this is due to the consumption of primary carbonate or dolomitic composition by hydrothermal neutralization reactions. The assumption is that carbonate was present before the primary chemical reaction described by Equation (1).

The Zebra rocks' unique gemstone quality hematite pattern is found in a relatively small area in the Western Australian East Kimberley region and has attracted heated attention (Loughnan & Roberts, 1990). Most Zebra rock patterns appear as reddish-brown stripes, rounded rods, and elliptical spots against the background. The red and brown structures have similar mineral compositions, while the latter is rich in ferric oxide concentration. Although the Zebra rock patterns were discovered and described over two centuries ago, an operative mechanism detailing their formation process is still lacking.

Previous investigations of the pattern-forming process in Zebra rocks include field, experimental, and theoretical analyses. In early studies, Larcombe (1924); Larcombe (1926) and Geidans (1981) suggested that the sedimentation processes, either in marine environments or ripple troughs, are responsible for the regular hematite precipitation based on the petrographic examination of Zebra rocks from the field. Hobson (1930) conducted a mineral analysis but found little evidence to support the theory of sedimentation without providing an alternative explanation. Later, Hancock (1968) proposed to explain the Zebra patterns by a post-depositional leaching theory. In his theory, groundwater circulation transports the iron and re-precipitates it into periodic patterns along the bedding and joint planes. However, the observation suggests a different mechanism as precipitation patterns also emerge in intact rocks.

Relevant studies have suggested potential chemical and hydrothermal environments during the pattern formation of Zebra rocks. Loughnan and Roberts (1990) proposed that the presence of dickite in some specimens is significant as it rules out a weathering alteration and points to an acid-sulfate alteration compatible with hydrothermal events as proposed by Kawahara et al. (2022). They found that pH-fluctuations induced by the oxidation decomposition of pyrite would create a favorable chemical environment to convert ferrous to colloidal hematite (Fe_2O_3). Hence, the concentration growth results in Liesegang striping due to the periodic coagulation of an autocatalytic nucleation mechanism. The proposed temperature of subsurface hydrothermal reactions may have been on the lower temperature spectrum following Abrajevitch et al. (2018) who suggest that the temperature never has been above 300°C. Retallack (2021) recently proposed that Zebra rocks may represent paleosol, which suggests that Ca and Mg are likely to be contained as major elements in the original conditions, supporting the possibility of acidic-hydrothermal alteration or chemical weathering near the surface.

The explanation of acidic-hydrothermal alteration is introduced by Kawahara et al. (2022) as traces of pyrite are found in Zebra rocks suggesting an acidic fluid environment. They thereby proposed a new formation mechanism arguing that the pH-fluctuations are due to the neutralization reactions between an Fe^{2+}-bearing acidic hydrothermal fluid and the carbonate minerals (dolomite) in the sedimentary rock (1). Accordingly, the Fe-precipitation

was postulated to form the characteristic rhythmic striping patterns in the wake of the iron concentration front. This model is coined as the Liesegang precipitation model.

Research questions raised by the above-described earlier studies include: (a) whether the pattern formation can be modeled by a quantitative description; (b) which mathematical model can be used to test predictions, and (c) how the variety of patterns observed in Zebra rocks can be reconciled with the Liesegang precipitation model. In particular, the transition to spotted patterns and the combined patterns with the bands and spots is not yet fully understood. More recent studies (Wang et al., 2015) on similar patterns have suggested that the Fe-bearing fluid's mass transfer rate is the cause. However, it is an open question which (THMCE) mass transfer mechanism is responsible for the pattern formation.

Therefore, we chose an approach with a thermodynamic generalized potential that can include chemical, mechanical, hydrological, thermal and electrically induced mass transfer processes for both phases. The advantage of this approach is that it allows a high level of abstraction through the focus on energetic processes. This minimizes the necessary assumptions about the mass transfer mechanisms and does not require the assumption of a specific thermodynamic driving force (e.g., a temperature gradient, pH-difference of the fluid or other chemical gradients, hydrostatic head, tectonic or overburden pressure and a difference in electrical potential). Instead, it offers the possibility to derive from the magnitude of the ratio of effective diffusion coefficients plausible causes for the mass transfer as will be discussed in Section 3 and applied to the presented Zebra band scenario in conclusion.

We first cast the Liesegang hypothesis into a concise thermodynamic basis following the classical Cahn-Hilliard description (Cahn & Hilliard, 1958) and subsequent modeling of Zebra rock pattern formations based on the Liesegang band theory. Several celebrated theoretical models have sought to describe the mechanism underlying the Liesegang phenomenon (Antal et al., 1998; Büki et al., 1995; Holba & Fusek, 2000; Ostwald, 1902) since it was first described at the end of 19th century (Liesegang, 1906). However, a concise mechanism that could summarize the complex processes involved—without special emphasis on thermodynamics laws—does not yet exist in the literature. Here we employ and elaborate on a phase separation theory introduced two decades ago (Antal et al., 1999, 2001). In this model, pattern formation appears due to spontaneous phase separation (unmixing) of the mixture in the presence of small fluctuations, that is, system noise (Gómez et al., 2008; Vignal et al., 2017).

The phase separation model underlying the Cahn-Hilliard dynamics is widely used for its simple concept and capability of simulating irregular patterns and the transition between stripes and spots (Dayeh et al., 2014; Hantz & Biró, 2006; Liu et al., 2022; Thomas et al., 2013). The formulation has been widely adopted in many fields through its early application to efficient modeling of the evolution of phase separation in binary alloys. This process is known as "spinodal decomposition." For the Liesegang patterning, it has been interpreted as a discrete scenario of competing dynamics between spin-flip (i.e., reaction) and spin-exchange (i.e., diffusion) (Antal et al., 1999), evolving toward the final stationary pattern. It is worth noting that this category of generalized approach has gained significant success in diverse disciplines, including those involving morphogenesis in a system of natural materials (Arguello, Gumulya, et al., 2022; Arguello, Labanda, et al., 2022; Arguello et al., 2023; Christoph et al., 1999; Cooper, 2012; Nakouzi & Sultan, 2011), and those focusing on digital pattern recognition in for example, (Bertozzi et al., 2007; Theljani et al., 2020), due to the striking similarity in the essential force-flux interactions of thermodynamic nature. Here, the concept of phase separation is employed for interpretation and parameter inversion of the rhythmically banded and spotted patterns of East Kimberley Zebra rocks, which can be extended to the general classification of Mississippi Valley Type deposits (L'Heureux, 2013; Kelka et al., 2017).

In the following, we present the basic methodology, introduce the numerical approach (a validation against empirical experimental results can be found in the Appendix) and proceed to model the specific Liesegang pattern observed in Zebra rocks. We show that the striped patterns, developed perpendicular to the propagating front of the reactants, can be inverted to derive the diffusion coefficients in the Cahn-Hilliard formulation. The transition to the spotted pattern is only discussed qualitatively in this work. In the discussion, we interpret the resulting diffusion coefficients regarding the complex multiphysics processes involved. In conclusion, we highlight the potential future use of the numerical platform developed in the present paper.

2. Methodology

Patterns in rock formations have attracted intense interest in the literature and have been identified to be caused by simple, local interactions between many components of a reaction-diffusion system giving rise to a diverse
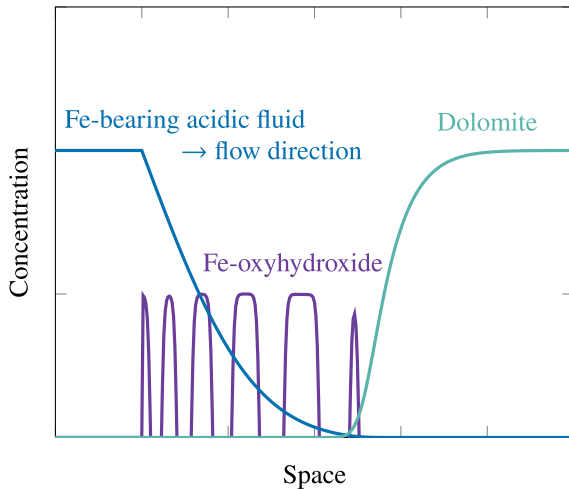
Figure 1. Sketch of diffusion fronts, fluid flow direction and rhythmic precipitation of Fe-Oxyhydroxide.

range of structures such as foliations and lineations produced by metamorphic differentiation, micro- to regional scale fracture systems, compaction bands and shear bands (Behnoudfar et al., 2022; Fei et al., 2022; Hobbs et al., 2011). The local interactions can be identified in many cases, but their exact interplay can hardly be quantified (Cier et al., 2022).

We propose to first test a simple approach that delivers stationary patterns from a scenario of a mixture of merely two components that move against the concentration gradients to form pure components in each phase after decomposition. The thermodynamic gradients are assumed to be driven by a double-well energy landscape (Figure 2) accounting for bulk energy density and the generated interfacial energy density by the movement. The bulk energy is a function of the concentrations, whereas the interfacial energy depends on the concentration gradients.

This generic formulation has been used for many pattern-forming processes, such as in recent studies on porous media (Cirillo et al., 2013) and granular matter (Li et al., 2021). The formulation does not incorporate dynamic interaction between the two phases as formulated in the enriched cross-diffusion formulation (Hu et al., 2020; Regenauer-Lieb et al., 2021). However, the essential time evolution of the above binary mixture of iron-rich solution and the hematite precipitate (1) under a reaction-self-diffusion process is captured in a thermodynamically consistent way. The pattern-forming process relies on a simple rule that the system evolves to either of the two minima of the free energy function, creating the so-called spinodal decomposition reaction by spontaneous unmixing (Gómez et al., 2008).

The basic assumptions are (a) the pattern forms in a two-phase system with self-diffusion accompanying the reaction of Equation 1; (b) the iron-rich fluid is transferred by an unknown mass transport mechanism through the low porosity dolomite-bearing sandstone (diffusion direction and precipitation process shown in Figure 1); (c) the generation of new surfaces due to Fe-precipitation is the only energy sink; (d) the reaction driven by the reduction in free energy obeys the biharmonic operator in the Cahn-Hilliard formulation; (e) the decomposition process evolves toward a stationary pattern at the infinite time limit (i.e., fully established band pattern).
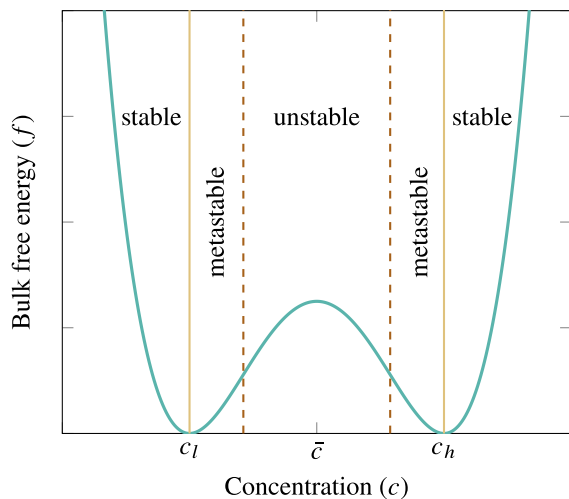
2.1. Phase Separation Model

The classical phase separation concept is adopted here to explain the Liesegang pattern formation in a reaction-diffusion system. Generically, we consider two reagents A and B (Fe-bearing acidic fluid and dolomite, respectively, in the current study; see (1)) that react, producing C (i.e., Fe-Oxyhydroxide) in the wake of a moving diffusion front: $A + B \rightarrow C$, defined as a second-order, as the only irreversible reaction in the system, illustrated in Figure 1. The illustration follows the schematics first proposed by Sultan et al. (1990) to explain the similar precipitation mechanism of goethite minerals later also applied to analogous deposition of $CaSO_4$ by Al-Ghoul and Sultan (2019). The corresponding two reaction-diffusion equations read

$$\begin{aligned}\frac{\partial a}{\partial t} &= D_a \ \Delta a - \kappa ab \\ \frac{\partial b}{\partial t} &= D_b \ \Delta b - \kappa ab\end{aligned} \qquad (2)$$

where a and b denote the concentration of the reagents A (Fe-bearing acidic fluid) and B (dolomite). Δ is the Laplacian, κ the reaction rate, and D_a and D_b the effective diffusion coefficient of the acid into the solid matrix and that of the dissolved dolomite in the fluid phase, respectively.

Figure 2. Sketch of double-well bulk free energy profile against concentration, with two minima at c_l and c_h and one maximum at $\bar{c} = (c_l + c_h)/2$. Two dashed lines indicate the spinodal values. The system is unstable between these two values and experiences phase separation.

The phase separation model assumes that the reaction product C separates into two distinct phases: low- and high-concentration phases, without forming intermediate complexes (Antal et al., 1999). The concentration contrast between phases leads to the forming of precipitation patterns. In this study, the generated Fe-Oxyhydroxide concentration enters an unstable region (known as the spinodal), where it divides into a low-concentration region (no precipitate) and a high-concentration region (precipitate), which is underpinned by the Cahn-Hilliard equation (Cahn, 1961; Cahn & Hilliard, 1958):

$$\frac{\partial c}{\partial t} = \nabla \cdot (\lambda \nabla \mu) + \kappa ab + \eta_c \tag{3}$$

where c denotes the concentration of the reaction product C (the precipitate), λ the mobility of the product. κab represents the rate of production of C particles at the reaction-diffusion front, and η_c denotes possible noise effects, including the inhomogeneity introduced by the initial concentration of constituents, thermal fluctuation of the system, influx from the environment, etc.; μ is the total free energy density characterized by a generalized chemical potential (Cahn & Hilliard, 1958) that drives the phase separation, which consists of two components: the bulk free energy density $f_{,c}$ and the interfacial energy density $\sigma \Delta c$ written as

$$\mu = f_{,c} - \sigma \Delta c \tag{4}$$

in which σ is the gradient parameter related to the thickness of the interface. f and $f_{,c}$ are the bulk free energy and its density, respectively. When reactions cause the material to spontaneously separate into solid and fluid phases, an effective nonequilibrium chemical potential needs to be formulated to account for the potential microscopic violation of the action-reaction symmetry. We are here using a phase-separation model that leads to stationary patterns formed in Zebra rocks in the infinite time limit. This is equivalent to a coarse-graining of the dynamic behavior in the form of excitation waves expected from the reaction-cross-diffusion approach with micro-physics enrichment (Hu et al., 2022; Regenauer-Lieb et al., 2021; Sun et al., 2022).

The bulk free energy f of the system has two minima in the equilibrium states, associated with the low and high concentrations (denoted as c_l and c_h, respectively) of the production of precipitates. For simplicity, we use a Landau-Ginzburg double-well free energy f with the minima at c_l and c_h and the maximum $\bar{c} = (c_l + c_h)/2$ as shown in Figure 2.

$$f = -\frac{\varepsilon}{2}(c - \bar{c})^2 + \frac{\gamma}{4}(c - \bar{c})^4 \tag{5}$$

where ε and γ are system-dependent parameters and $\sqrt{\varepsilon/\gamma}$ determines the minima of the bulk free energy f. Both $\varepsilon > 0$ and $\gamma > 0$ are required (see Figure 2) to induce phase separation in the system.

The generalized chemical potential hence writes as

$$\mu = -\varepsilon(c - \bar{c}) + \gamma(c - \bar{c})^3 - \sigma \Delta c \tag{6}$$

We rewrite (2) and (3) in a dimensionless form by defining the normalized concentration, time, and length scales as

$$\hat{c} = \frac{c_h - c_l}{2}, \quad \tau = \frac{1}{k\hat{c}}, \quad l = \sqrt{\frac{D}{k\hat{c}}} b \tag{7}$$

and shifting the normalized concentration as

$$m = \frac{c - \bar{c}}{\hat{c}} \approx \frac{c}{\hat{c}} - 1. \tag{8}$$

Coupling Equations 2–4, we obtain the dimensionless final set of equations governing the pattern-forming process:

$$\begin{aligned} \frac{\partial a}{\partial t} &= D_a \ \Delta a - \kappa ab \\ \frac{\partial b}{\partial t} &= D_b \ \Delta b - \kappa ab \\ \frac{\partial m}{\partial t} &= \nabla \cdot (\lambda \nabla \mu) + \kappa ab + \eta_c \\ \mu &= -\varepsilon m + \gamma m^3 - \sigma \Delta m \end{aligned} \tag{9}$$

where $\sigma = \sigma_0 k\hat{c}/D\varepsilon$ denotes the normalized gradient parameter. Note that $\lambda = \lambda_0 \varepsilon/D$ and $\eta_c = \eta_{c0}/k\hat{c}^2$ are now redefined as the normalized mobility, and normalized noise parameter, of the product (Fe-oxyhydroxide), respectively.

2.2. Definition of the Numerical Experiment

The above-described phase separation approach is cast into a numerical experiment with the following definition of system variables. a corresponds to the concentration of the Fe-bearing acidic fluid in Equation (1) and b to the dolomite concentration and m the Fe-Oxyhydroxide precipitate as a normalized concentration of the product. D_a and D_b are the diffusion coefficients of acidic fluid and dolomite reactants, respectively. The reaction rate depends on the rate constant κ and on the concentration of the two reactants (see Figure 1). The experiment is based on the principle of mass conservation leading to the problem definition described as follows.

We consider a 2D initial–boundary value problem in a rectangular domain Ω where the domain boundary is denoted by Γ with a unit outward normal vector $\mathbf{n}$. We prescribe the essential boundary conditions for the primary variables, that is, the concentration of the two reagents and the product, and the generalized chemical potential μ, with their domain boundaries as Γ_a, Γ_b, Γ_m, and Γ_μ, and the respective natural boundaries Γ_p, Γ_q, Γ_r, and Γ_t.

The essential and natural boundary conditions imposed on the system are hence described as

$$a = \bar{a} \text{ on } \Gamma_a; \;\; b = \bar{b} \text{ on } \Gamma_b; \;\; m = \bar{m} \text{ on } \Gamma_m; \;\; \mu = \bar{\mu} \text{ on } \Gamma_\mu \tag{10}$$

and

$$\nabla a \cdot \mathbf{n} = j_a \text{ on } \Gamma_p; \;\; \nabla b \cdot \mathbf{n} = j_b \text{ on } \Gamma_q;$$
$$\nabla m \cdot \mathbf{n} = j_m \text{ on } \Gamma_r; \;\; \nabla \mu \cdot \mathbf{n} = j_\mu \text{ on } \Gamma_t, \tag{11}$$

respectively.

The decomposed boundaries satisfy

$$\overline{\Gamma_a \cap \Gamma_p} = \overline{\Gamma_b \cap \Gamma_q} = \overline{\Gamma_m \cap \Gamma_r} = \overline{\Gamma_\mu \cap \Gamma_t} = \emptyset$$
$$\overline{\Gamma_a \cup \Gamma_p} = \overline{\Gamma_b \cup \Gamma_q} = \overline{\Gamma_m \cup \Gamma_r} = \overline{\Gamma_\mu \cup \Gamma_t} = \Gamma \tag{12}$$

Their corresponding initial conditions are assumed as constant, written as

$$a|_{t=0} = a_0; \;\; b|_{t=0} = b_0; \;\; m|_{t=0} = m_0; \;\; \mu|_{t=0} = \mu_0 \quad \text{in } \Omega. \tag{13}$$

Although we do not restrict our analysis with additional assumptions, we identify the slowest thermodynamic process for a parametric study (in Section 2.3) as a first guess to fit the observed patterns. For this, we assume that the process is rate-limited by the dissolution reaction of the dolomite with the weak acidic solution, implying a slow process; see the reaction and precipitation rates described in Deike (1990) and Yoshida et al. (2020). A simplification adopted is therefore, to neglect the advective transport in the system and investigate the possible source mechanism of the pattern-forming process as an evolution resulting from multiphysics thermodynamic force and flux interactions. Following the assumption of chemical dissolution as the slowest possible thermodynamic process among other physics, it is also assumed that the thermodynamic force resulting from boundary conditions imposed on the numerical model drives the system through the concentration gradients. We remove hence assume zero flux on the bottom boundary and set a constant concentration of the acidic Fe-bearing fluid source on the top boundary as specified in the Appendix. The initial condition throughout the system is a pristine (i.e., no acid-bearing fluid) dolomite-containing protolith, implying that the presence of Fe-bearing acidic fluid is externally derived. There is no Fe-Oxyhydroxide in the formation prior to the incoming fluid reacting with the dolomite. The Appendix also introduces the weak form solution required for the finite element implementation.

The numerical formulation reproduces the empirical laws from previous experimental studies as described in the Appendix (Nabika et al., 2019). This demonstrates that the numerical model provides a robust platform for the inversion of diffusivities from field observations. In the next Section 2.3, we perform a parametric study of the effect of diffusion coefficients on the spacing law, which is linear or nonlinear depending on the type of diffusion process, to obtain a direct derivation of the diffusion coefficients. The key diffusion coefficients include the ratio of the self-diffusion coefficients D_a/D_b and the Cahn-Hilliard mobility λ. In the subsequent sections, we present the numerical study of the diverse patterns simulated for Zebra rocks, that is, regular stripes (including uniform stripes) in Section 2.4 and irregular patterns containing stripes and spots in Section 2.5.
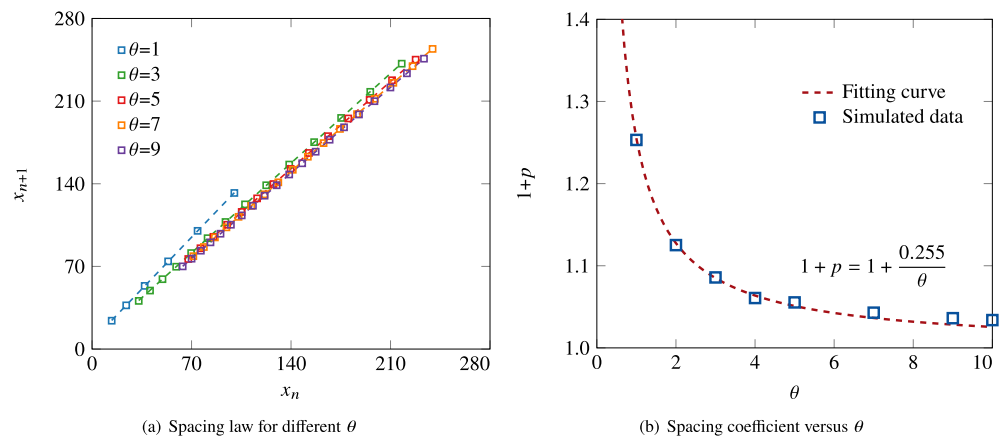
(a) Spacing law for different θ

(b) Spacing coefficient versus θ

Figure 3. Spacing laws for different self-diffusion coefficient ratios $\theta = 1, 2, 3, 4, 5, 7, 9, 10$: (a) spacing laws for different θ and (b) spacing coefficients versus θ.

2.3. Diffusion Coefficients

Three diffusion coefficients appear in the governing Equation 9: the self-diffusion coefficients D_a which describes a hydrodynamic dispersion (sum of the diffusion and dispersion multiphysics processes) of the Fe-bearing fluid A and D_b the diffusion associated with the dissolution of dissoluble dolomite B and mobility λ of the reaction product C (Fe-Oxyhydroxide). The self-diffusion coefficient ratio $\theta = D_a/D_b$ parametrizes the influence of these self-diffusion coefficients of the reagents. The parameter study is performed for diffusion coefficients $D_a > D_b$ as the dissolution of dolomite into acidic solution is commonly held to be smaller than the diffusion of hydrogen through the rock matrix. Thus, we vary D_a and λ, with fixed $D_b = 1$ in our studies. Figure 3 displays the spacing laws in terms of $\theta = 1, 2, 3, 4, 5, 7, 9$ and 10. The figures show that as θ grows the spacing coefficient $1 + p$ drops. We correlate the parameters θ and $1 + p$ ($= x_{n+1}/x_n$, as shown in the Appendix) by plotting the ratio of the self-diffusion coefficients vs. the spacing coefficient, see Figure 3b.

Our results confirm that the spacing coefficient is in a hyperbolic relationship with the ratio of self-diffusion coefficients, as reported by Itatani et al. (2021). A high diffusivity ratio θ effectively decreases the distance between adjacent stripes, as the phenomenological Matalon-Packter law predicts (Kulkarni et al., 2022; Matalon & Packter, 1955). The Matalon-Packter law associates the parameter p with the initial concentration of the reagents A and B as stated in the Appendix. Increasing the diffusion coefficient D_a is equivalent to raising the concentration of the incoming reagent A, decreasing p and the relative thickness of the stripes. Analogizing the phenomenological Matalon-Packter law, we fit the nonlinear numerical results using a hyperbola

$$1 + p = 1 + \frac{0.255}{\theta}$$

This allows us to determine the self-diffusion coefficient ratio from field measurements of Zebra rock patterns.

We analyze the effect of Cahn-Hilliard dynamics on the spacing by sampling λ between 0.1 and 0.9 with 0.2 increments. Figure 4 depicts the spacing coefficients $1 + p$ for different λ values. Contrary to the self-diffusivities, a high Cahn-Hilliard mobility of the product λ increases the spacing, where the increment is linear as Figure 4b shows

$$1 + p = 1.01 + 0.25\lambda$$

This linear relationship is of potential interest to geological and industrial applications. For instance, once we measure the spacing coefficient of a given sample, we can calibrate λ to match the existing Liesegang patterns. Given the key factors affecting λ in experiments and geological applications, we optimize the process to achieve the expected Liesegang patterns.

2.4. Liesegang Stripes in Zebra Rocks

In this section, we analyze the regular patterns appearing in Zebra rocks quantitatively. The distinct Zebra patterns are associated with the interaction between the diffusion and reaction processes. In this study, we assume the reac-
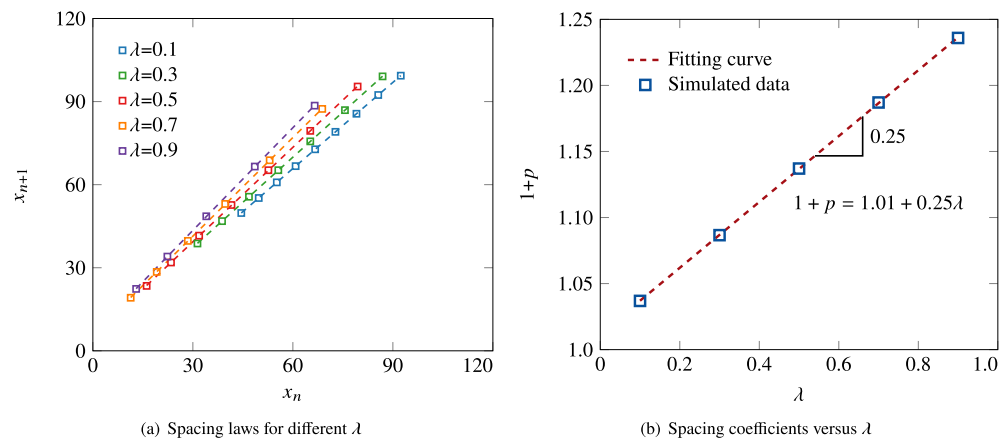
(a) Spacing laws for different λ

(b) Spacing coefficients versus λ

Figure 4. Spacing laws for different Cahn-Hilliard mobilities $\lambda = 0.1, 0.3, 0.5, 0.7, 0.9$: (a) spacing laws for different λ and (b) spacing coefficients versus λ.

tion rate constant and vary the diffusion coefficients by modifying either the ratio of self-diffusion coefficients or the Cahn-Hilliard mobility. For a given Zebra rock sample, we first measure the spacing coefficient $1 + p$ as listed in Table 1. The measured $1 + p$ enables us to estimate the corresponding combinations of the self-diffusion ratio θ and the Cahn-Hilliard mobility λ. Finally, we rely on our numerical model with varying combinations of coefficients to fit the Zebra patterns. We report four examples of Zebra rock samples being successfully reproduced with optimized coefficients, as follows.

For the Zebra rock sample 1 in Figure 5 from Mattievich et al. (2003), we find that the formed patterns follow both the spacing and width laws as shown in Figure 6. We scale the band position x_n and its width w_n by a chosen cross-section whose length is represented by the green axis in Figure 5 and fit the measured data as a linear line. The slope corresponding to the spacing coefficient is estimated to be around 1.071. Also, $1 + p = 1.071$ corresponds to a λ in the range of 0.1–0.3 based on Figure 4b when fixing the ratio of self-diffusion coefficient $\theta = 1.0$. After choosing the combination $\theta = 1.0$ and $\lambda = 0.244$ based on the linear relationship $1 + p = 1.01 + 0.25\lambda$, the numerical results show a good agreement with the Zebra rock sample with reference to the formed patterns, as demonstrated in Figure 5. This similarity is also found in Figure 6a where the simulated band locations match with the measured band locations. The fitting curve based on the simulated data yields a high R-square value $R^2 = 0.99$, indicating a strong linear relationship of the spacing law reproduced by our numerical results. In addition, we compare the thickness of the measured stripes and the simulated stripes. Given the variation in the measured thickness of the natural stripe patterns, we plot the scaled measured widths with standard deviations. Figure 6b shows that the difference between the simulated and measured width is within an acceptable range.

In what follows, we use two Zebra rock samples from the Western Australian Museum (see Figures 7a and 9a) to quantitatively investigate the effect of the self-diffusion coefficients. As the diffusion fronts are not one-dimensional in both samples, indicated by the curved stripes, we draw a curved green axis along the normal direction of each band to approximate the principal diffusion direction. Figures 7b and 9b represent the Liesegang stripes along the curved cross-sections allowing to estimate the spacing coefficients. The measured spacing coefficients $1 + p$ are 1.060 and 1.054, respectively, for the Zebra rock samples 2 and 3. Thus, according to Figure 3b, we choose the ratio of self-diffusion coefficients $\theta = 4.25$ and 4.72 while fixing the Cahn-Hilliard mobility $\lambda = 1.0$. Figures 8 and 10 show that the simulated spacing and width laws are nearly identical to those from Zebra rock sample measurements when using the estimated parameters.

Table 1
Measured Spacing Coefficients and Estimated Self-Diffusion Coefficients and Cahn-Hilliard Mobilities for Four Zebra Rock Samples

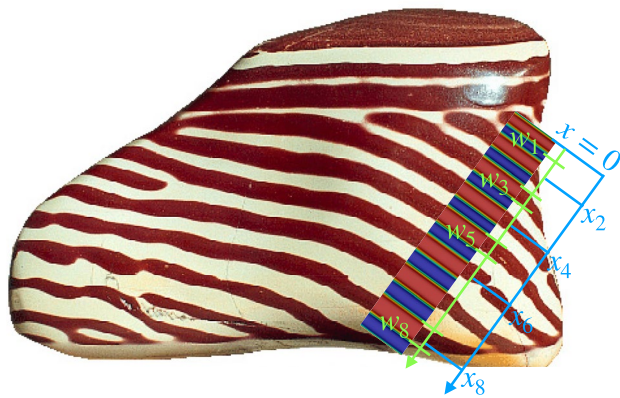| Sample number	1	2	3	4
Measured spacing coefficients $1 + p$	1.071	1.060	1.054	1.000
Estimated ratios of self-diffusion coefficients θ	1.0	4.25	4.72	7.0
Estimated Cahn-Hilliard mobilities λ	0.244	1.0	1.0	0.1

Figure 5. Pattern comparison between the simulated results and the Zebra rock sample 1 modified from Mattievich et al. (2003).

As a special end-member uniform constant width and spacing patterns are observed in Zebra rocks, as Figure 11 exemplifies. This may indicate the tendency for the Zebra rock patterns to form under very slow dynamic processes close to the ideal stationary Turing pattern (slope zero on the width law in Figure 11b). The uniform pattern also implies negligible variations between stripes, indicating the spacing coefficient is $1 + p \approx 1$, following the classical Turing pattern (see steady wave solutions in Hu et al. (2022)). As Figures 3b and 4b suggest, a combination of the large ratio of the self-diffusion coefficient θ and the small Cahn-Hilliard mobility λ generates a small spacing coefficient. Here, setting $\theta = 7.0$ and $\lambda = 0.1$ can reproduce the regular pattern, matching the data derived from the images as Figure 12 presents. We, therefore, conclude that our working hypothesis that the Liesegang pattern can be directly used for the derivation of key physical parameters using for example, simple computer-vision analysis, is proven.

2.5. Transition From Stripes to Spots in Zebra Rocks

In addition to the regular and uniform Liesegang stripes arising in Zebra rocks, there are two other categories of irregular patterns; these are patterns with intermixed stripes and spots and pure spotted patterns as Figures 13a and 13b and Figure 13c show, respectively. The physical reason for the transition between stripes and spots in Zebra rocks is not uniquely identified in the literature. In this section, we present a first-step numerical investigation of the role that the mobility λ plays in generating diverse patterns. Figures 13a–13c illustrate the three stages of the transition: (a) stripes separating into connected spots, as shown in Figure 13a, (b) followed by partly connected spots, as observed in Figure 13b, and (c) the full development into isolated spots, see Figure 13c.

Based on the phase separation model, three parameters control the transition from stripes to spots in a reaction-diffusion system (Al-Ghoul et al., 2009; Dayeh et al., 2014; Wang et al., 2015), namely, the Cahn-Hilliard mobility λ, the noise distribution η_c, and the initial reagent concentration distribution. A random noise η_c with a uniform distribution in $[-0.01, 0.01]$ is applied to Equation 9 as the imposed system inhomogeneity. We vary λ and the initial distribution of reagents to capture Liesegang striping in irregular Zebra patterns, containing both spots and stripes.

To reduce the computational cost, the system size is set to half of the 2D scenario, $L_x = 160$ and $L_y = 32$ with a uniform grid $1{,}280 \times 256$ in the x- and y-directions, respectively, and the time step increases two times to $\Delta t = 5 \times 10^{-5}$. Modified parameters compared to those given in Appendix A2 include $\gamma = 0.15$, the initial condition $b_0 = 0.5$ and $m_0 = -1.5$. Figure 14 displays the simulation results of the product distribution patterns for λ varying from 0.1 to 0.6 with a 0.1 increment at the same time $t = 200$, respectively. A combination of spotted and striped patterns is shown in all patterns with the trend of a smaller λ leading to a smaller size (and hence

(a) Measured and simulated spacing laws

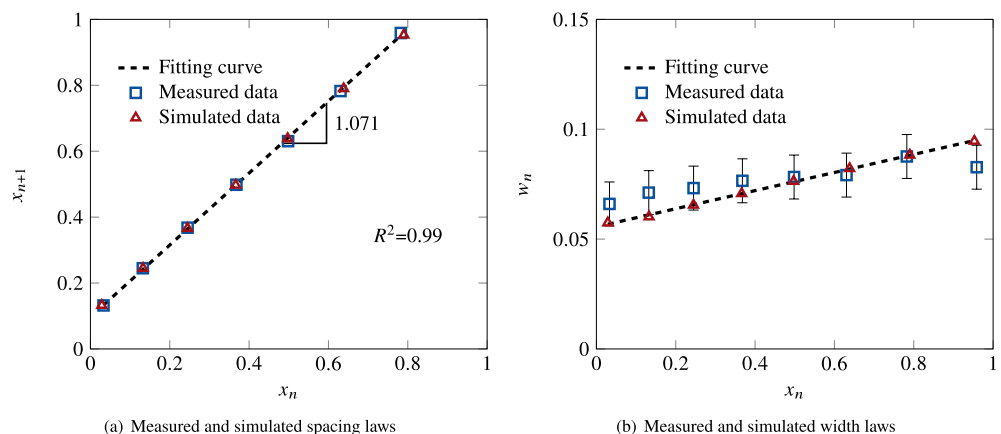(b) Measured and simulated width laws

Figure 6. Comparison between the Zebra rock sample 1 and its numerical results for (a) spacing and (b) width laws.
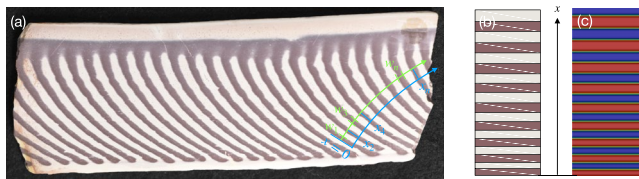
Figure 7. (a) Zebra rock sample 2, (b) measured stripes along the curved diffusion direction, and (c) simulated bands.

denser distribution) of spots. For example, the $\lambda = 0.1$ case resembles the fully developed spotted pattern in Figure 13c. For larger values of $\lambda \geq 0.2$, the transition from stripes to spots is less complete as a higher mobility of the product essentially promotes Ostwald ripening.

Figure 15 further shows the time evolution of the pattern-forming process for the case $\lambda = 0.2$ from $t = 100$ to $t = 250$, revealing the time-lapse transition from stripes to spots. It is observed that as time progresses part of the stripes gradually localize into spots as a result of the imposed heterogeneity. Later on (from $t = 200$ to $t = 250$) we note an interesting feature that the evolution of these localized spots pattern is overtaken by the Ostwald ripening effect.

Overall, we find the trend that for cases of $\lambda < 0.2$, the phenomenon of stripes localizing into spots is prominent over the entire domain while for cases of $\lambda \geq 0.2$, such type of localization instability is regional, Ostwald ripening dominates over localization at a global scale.

3. On the Effective Diffusion Coefficients: A Multiphysics Interpretation

This paper describes the Liesegang striping process using a phase-field model that is representative for a plethora of rhythmic mineralization patterns. The working hypothesis uses the Cahn-Hilliard approach to quantitatively derive the diffusion coefficients of chemical species inside the rock mass. This proposition was based on the assumption that a generalized continuum approach to thermodynamic processes that captures the ensemble behavior of complex local interactions, can be used. The resulting framework is based on the dynamic interaction of thermodynamic forces and fluxes and their product defining the dissipative processes within the rock mass. This allows the use of a generalized chemical potential as the definition of the thermodynamic force and a generalized mass flux (Regenauer-Lieb et al., 2021) incorporating the Onsager Reciprocal Theorem. The specific physical meaning of the diffusivity and reaction coefficients is therefore not restricted to pure chemical-processes but can incorporate a multitude THMCE feedbacks which imply that the resulting diffusion coefficients are effective properties that may contain an averaging of spatio-temporal processes at lower scales in the dissipative system. Here we used the approach to model an apparent hydro-chemical system with other thermodynamic processes, potentially modulating the mixed dispersion-diffusion processes at a lower scale.

The underlying phase separation process of such patterns has the following fundamental property. Without the need to overcome a thermodynamic barrier required by nucleation mechanisms, they are, by definition, driven by the evolution of the local free energy of the interface between the phases on the background of a large-scale double-well free energy landscape (Cahn & Hilliard, 1958). The Cahn-Hilliard model is a fundamental generalized breakthrough in formulating a thermodynamically robust theory for pattern-forming processes that can be classified as a spontaneous internal unmixing problem. These pattern-forming processes in nature develop from small internal fluctuation inside the system and develop due to the internal mass exchange with competing diffusion processes. The Cahn-Hilliard mechanism provides a compelling perspective in the puzzle of understand-
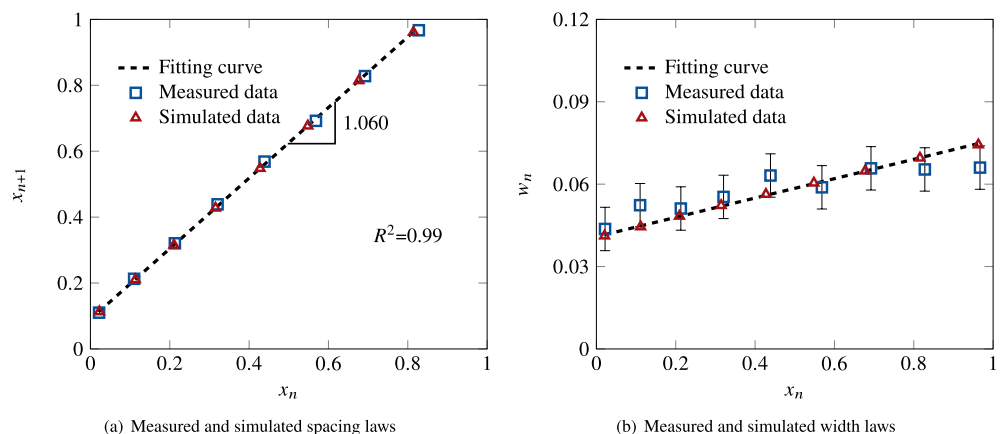

(a) Measured and simulated spacing laws

(b) Measured and simulated width laws

Figure 8. Comparison between the Zebra rock sample 2 and its numerical results for (a) spacing and (b) width laws.
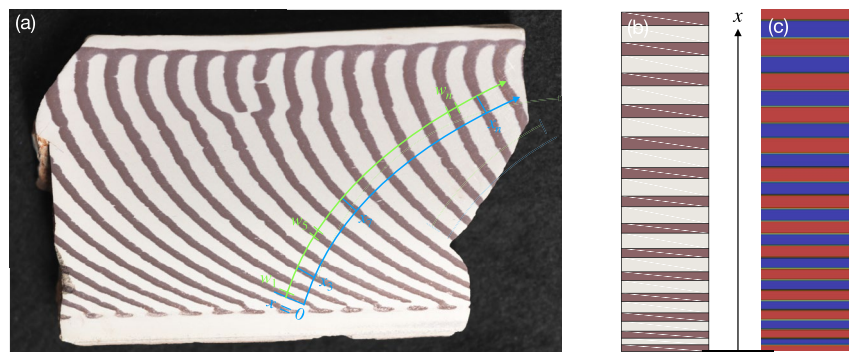
Figure 9. (a) Zebra rock sample 3, (b) measured stripes along the curved diffusion direction, and (c) simulated bands.

ing the unmixing process where thermodynamics appears to be defied and negative diffusion coefficients are required at the local scale (Haskell, 1973). This emphasizes the crucial role of the evolving interface between the two phases (here the iron-bearing acidic solution and the precipitation of the mineral Fe-Oxyhydroxide) which entails local interfacial energy and drives the process of spontaneous unmixing.

Specifically, we obtain in this study from the inversion of effective diffusion coefficients in the Zebra-stripe pattern extremely low ratios of diffusion of the Fe-bearing acidic fluid into the dolomite-bearing formation (θ close to unity) to four to seven times higher than the diffusion of the dissolved dolomite into the acidic fluid. This finding indicates that the solid and fluid mass transfer is indeed within the range of the slow dissolution of dolomite into the fluid. The low diffusion coefficient for the fluid flow D_a, being only up to an order larger than D_b, suggests that a likely thermodynamic driving force for mass movement is either an (electro-)chemical potential difference or a slow viscous material flow through a tight formation as induced by a stress gradient. The likelihood for the optional need of a mechanical driver of mass transfer (e.g., caused by overburden stress or tectonic forces) in the tight Zebra Rock formation provides a first quantitative proof from the thermodynamic perspective and may request a reinterpretation of the formation mechanism of other rhythmic mineralization patterns. This finding is extended here and could apply in principle to all Liesegang type patterns in geological rocks. The quantitative numerically assisted approach presented here can serve as a diagnostic tool to identify the mechanisms of formation.

In addition, the Cahn-Hilliard description of the phase separation is a generic phase separation model that encompasses the classical Turing pattern formation (perfectly rhythmic patterns found in some Zebra rocks) to the more Liesegang style pattern with the familiar scaling laws for distances and band widths and their mutual relationship as well as the possibility of formation of spotted patterns. Thus, it encompasses a wide range of observations and is, therefore a suitable approach when developing a generic method that does not presume a specific reaction-diffusion equation.
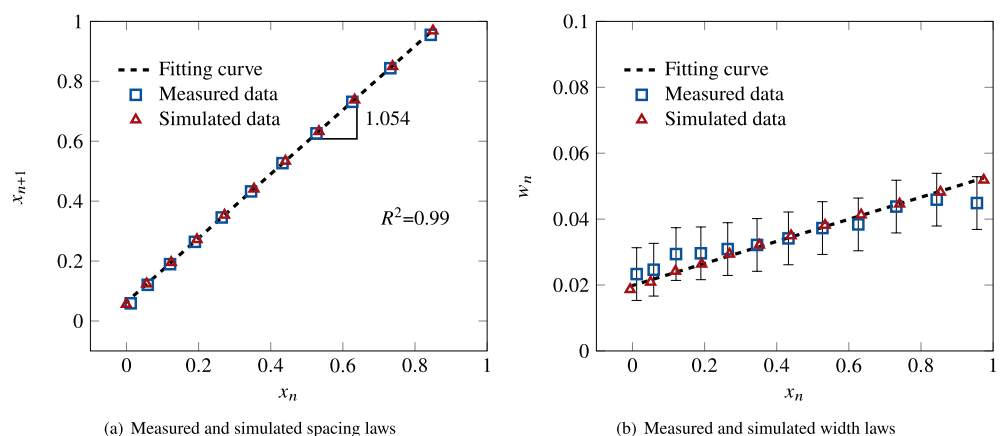

(a) Measured and simulated spacing laws

(b) Measured and simulated width laws

Figure 10. Comparison between the Zebra rock sample 3 and its numerical results for (a) spacing and (b) width laws.
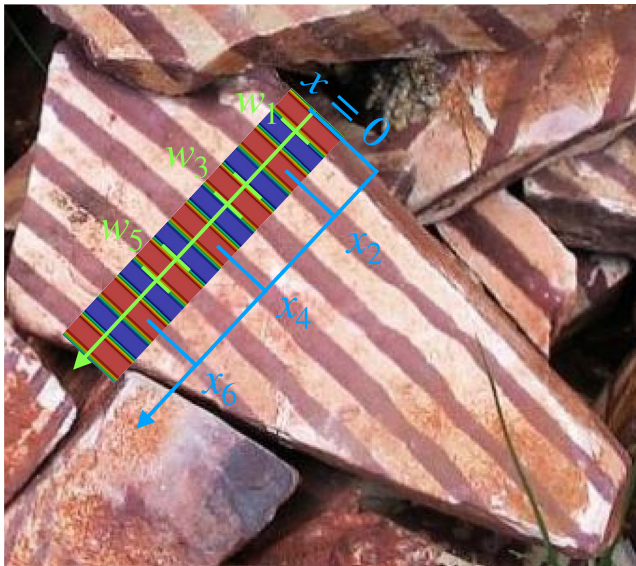
Figure 11. Pattern comparison between the Zebra rock sample 4 and its numerical results.

4. Conclusions

Phase separation in Zebra rock is found to have developed spontaneously from local perturbations toward a frozen-in tessellated geometry. Pattern may therefore be interpreted as a "bar code" equivalent of their internal reaction-diffusion coefficients. In this work, we have examined the possible application to the inversion of diffusion coefficients from rhythmic patterns observed in rocks. We find that the diffusion coefficients, including self-diffusion coefficients and Cahn-Hilliard mobility, significantly affect the pattern spacing and width, thereby offering a quantitative analysis tool for a given reaction-diffusion system, specifically for the case of regular Zebra rock patterns, which is here modeled in pseudo-1D for computational efficiency with demonstrated accuracy.

In earlier numerical studies, the dynamics of Ostwald ripening between the leading front and the trailing bands of the propagating dissolution-precipitation reaction front was proposed to lead to the observed scaling behavior and mass oscillation in the bands (Mansour & Al-Ghoul, 2015). This earlier numerical analysis also uses a reaction-diffusion formalism but employs an arbitrary Heaviside function to prevent the total dissolution of the precipitation bands formed by the reaction product (here hematite). Our model refines this simplification and considers the reaction product mobility governing the double-well kinetics of the spinodal decomposition in the Cahn-Hilliard approach to prevent the total dissolution of the bands. This inclusion of additional dynamics does not appear to change the qualitative findings of the numerical earlier studies but is essential for quantitative inversion of the dynamic parameters. For low mobility values, this can lead in particular to the phenomenon of a transition from bands to spots which is not captured by the Heaviside function approach. The inclusion of Cahn-Hilliard dynamics is therefore an important ingredient for a simple model of the pattern formation in Zebra rock.

Periodic precipitation bands with increasing width are generated as the reaction-diffusion front propagates, forming regular Liesegang band patterns. The numerical results are reproducing observations from controlled laboratory experiments supporting the argument that an approach based on material balances and first principles is a promising strategy for analysis of the empirical laws (Droz et al., 1999).

To model the transition of pattern evolution toward more complex and irregular geometries true 2D simulations were required. Of particular interest is the dynamic evolution from striped patterns into spot patterns or combined stripes and spots. For the transition from stripes to spots the magnitude of the Cahn-Hilliard mobility of the Fe-Oxyhydroxide reaction product is identified as a key parameter. This interesting dynamic phenomenon deserves future follow-up studies for quantitative inversion. In this study, we reproduced qualitatively a diverse set of spotted Zebra rock patterns by varying the Cahn-Hilliard mobility λ. For example, $\lambda < 0.2$ produces spotted

(a) Measured and simulated spacing laws
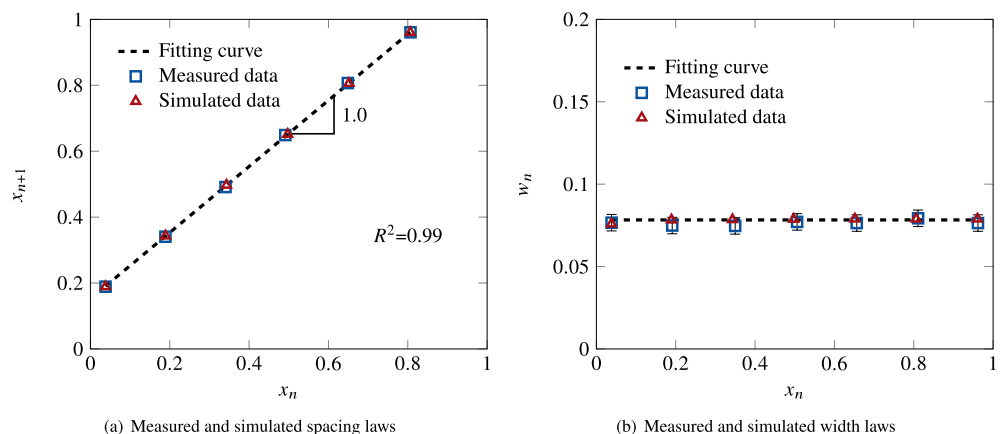

(b) Measured and simulated width laws

Figure 12. Comparison between the Zebra rock sample 4 and its numerical results for (a) spacing and (b) width laws.
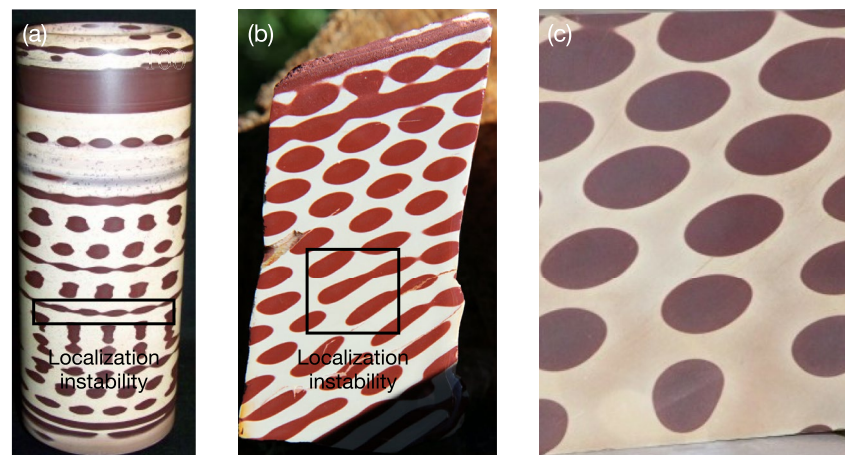
Figure 13. Stripe-to-spot transition in Zebra rocks: combined patterns with stripes and (a) connected spots and (b) partly connected spots, and (c) isolated spot patterns.

patterns, while for $\lambda \geq 0.2$, the patterns transition into a combination of stripes and spotted patterns. We therefore conclude that the Cahn-Hilliard mobility may be used in future studies to predict the transition patterns when both spots and stripes co-exist. For the case of regular Zebra bands the model allows us to accurately estimate effective diffusion coefficients from photographic evidence.

We obtain the interesting conclusion that the mass movement driving the Fe-bearing acidic fluid is unlikely to be a simple subsurface fluid flow driven by fluid pressure difference. Mass movements by electrochemical processes or slow mechanically forced fluid flows driven by the viscous deformation of the fine-grained matrix are more promising candidates. In more general terms our conclusion is that the thermodynamic driving force that causes the thermodynamic flux must lead to mass transfer which is on the same order of magnitude as the slow dissolution of dolomite. A mass transfer of the reactant acidic fluid driven by a critical combination of multiphysics processes is therefore proposed as a more robust conclusion. This is plausible considering the context of a hydrothermal environment composed of extremely fine-grained well-sorted quartz grains. The result may also explain the uniqueness of the clarity of the striping process in Zebra rock.

Further conclusions can be drawn from a closer analysis of the results. The direction of the mechanically or chemically assisted multiphysics flow can, for instance, be derived from the spacing. Periodic precipitation bands with increasing width are generated as the reaction-diffusion front propagates. The normalized values can be further quantified by additional chemical analyses (Kawahara et al., 2022). Such analyses can calibrate the image-based
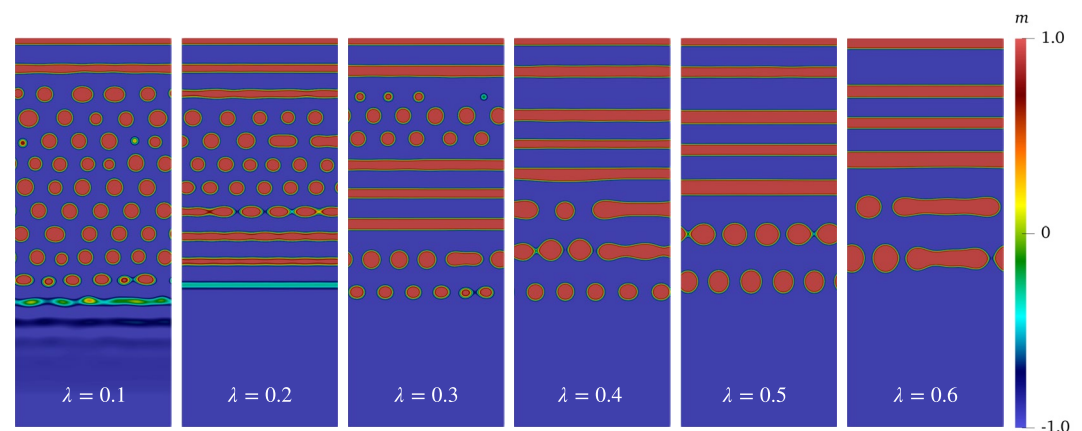

Figure 14. Stripe-to-spot transition for different Cahn-Hilliard mobilities ranging from 0.1 to 0.6 at $t = 200$ in the domain's upper half $L_x \in [0, 80]$. The scaled parameters used are $\bar{a} = 100$, $a_0 = 0$, $b_0 = 0.5$, $m_0 = -1.5$, $D_a = D_b = 1.0$, $\kappa = 1.0$, $\varepsilon = 1.0$, $\gamma = 0.15$, $\sigma = 0.2$, and $\eta_c \in [-0.01, 0.01]$.
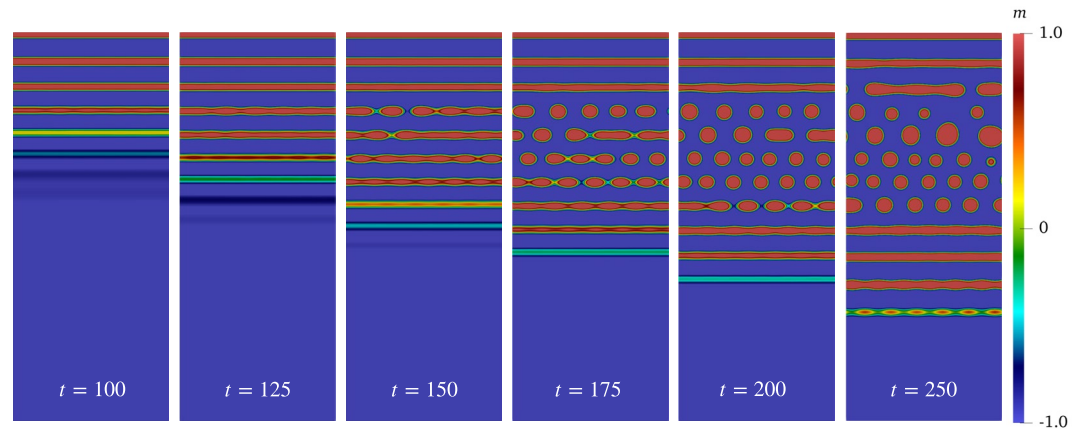
Figure 15. Localization instability triggers stripe-to-spot transition for $\lambda = 0.2$ in the domain's upper half $L_x \in [0, 80]$.

approach and turn non-dimensional values, as presented here, into dimensional properties for resource evaluation. Chemical analyses can also be used as an independent verification of maps of Fe-bearing fluid transport direction derived from image analyses using the width law in this study.

Additional information on the quantity of Fe-precipitation in the host rock can be derived from the spacing law. A combination of large ratios θ (high flux of Fe-bearing fluid) with small Cahn-Hilliard mobility λ of the reaction product Fe-Oxyhydroxide generates a small spacing coefficient add and consequently causes higher concentrations of iron in a unit rock mass. Low values of θ, on the contrary, imply low values of percolating Fe-bearing fluid and trigger a transition from bands to spots (Wang et al., 2015), implying low concentrations of iron per unit rock mass.

Future work will consider the assimilation of additional data to explain various geochemical and hydromechanical phenomena and predict potential energy and mineral resources. The formation of these striped patterns requires special redox conditions which were particularly favorable during the Archean, where commercially attractive banded iron formations were precipitated as sedimentary rocks (Condie, 2016). These resemble strongly the Zebra band patterns investigated here. The banded iron formations are laminated chemically reactive sediments that have an iron content larger than 15%–30%. They show distinct events in the time series of the Archean where following the great Earth oxidation event oxygen content in the seawater fluctuated strongly from basically anoxic at depth to strongly oxidated following a glaciation event (Holland, 2006). A thorough investigation of their style with our model might be developed into an outcrop exploration tool of expected grades and Fe-bearing fluid transport direction conveniently based on aerial photographs or drone images. Moreover, if the method can be used with confidence to identify concentration gradients pointing to high-grade ores, the numerical workflow as presented here can help in quantifying and optimizing resource recovery with energy and cost savings for recovery, transport and crushing. The finding that the basic width, spacing and Matalon-Pakter laws can be reliably inverted from the observed images using relatively coarse meshes offers future opportunities to open an entirely new scope of geophysical field exploration techniques.

Appendix A

A1. Finite Element Formulation

We solve the coupled nonlinear partial differential Equation 9 using an open-source high-performance phase-field code, PRISMS-PF (DeWitt et al., 2020) based on the finite element library of deal.II (Arndt et al., 2020). The library supports adaptive mesh refinement, massively parallel, and matrix-free finite element simulation. We derive the weak formulation to the coupled Equation 9 with the boundary and initial conditions (10)–(13) using the following trial functions

$$S_i := \left\{ i : \Omega \to \mathbb{R} \mid i \in H^1, \; i = \bar{i} \text{ on } \Gamma_i \right\}, \; i \in \{a, b, m, \mu\}$$

and test functions

$$\mathcal{V}_j := \left\{ j : \Omega \to \mathbb{R} \mid j \in H^1, \, j = 0 \text{ on } \Gamma_j \right\}, \, j \in \{\phi, \psi, \eta, \omega\}$$

and integration by parts. By adopting the forward Euler method for time discretization, the corresponding weak forms become

$$\int_\Omega \phi a^{n+1} \, dV = \int_\Omega \phi \underbrace{(a^n - \Delta t \kappa a^n b^n)}_{r_a} - \nabla \phi \underbrace{\Delta t D_a \, \cdot (\nabla a^n)}_{r_{ax}} \, dV \tag{A1}$$

$$+ \int_\Gamma \phi (\Delta t D_a) j_a^n \, dS$$

$$\int_\Omega \psi b^{n+1} \, dV = \int_\Omega \psi \underbrace{(b^n - \Delta t \kappa a^n b^n)}_{r_b} - \nabla \psi \underbrace{\Delta t D_b \, \cdot (\nabla b^n)}_{r_{bx}} \, dV \tag{A2}$$

$$+ \int_\Gamma \psi (\Delta t D_b) j_b^n \, dS$$

$$\int_\Omega \omega m^{n+1} \, dV = \int_\Omega \omega \underbrace{(m^n + \Delta t \kappa a^n b^n + \Delta t \eta_c)}_{r_m} - \nabla \omega \underbrace{\Delta t \, \cdot (\lambda \nabla \mu^n)}_{r_{mx}} \, dV \tag{A3}$$

$$\int_\Omega \eta \mu^{n+1} \, dV = \int_\Omega \eta \underbrace{\left(-\epsilon m^n + \gamma (m^n)^3\right)}_{r_\mu} + \nabla \eta \cdot \underbrace{\sigma \nabla m^n}_{r_{\mu x}} \, dV \tag{A4}$$

The numerical analysis presented as follows is based on an implementation of Equations A1–A4 in PRISMS-PF, which allows for future extensions of this study to a 3D scenario with its adaptive mesh refinement feature.

A2. Numerical Validation Against Empirical Laws

We validate the numerical results with experimentally derived findings of the Liesegang striping which is cast into four empirical laws, the width law, the spacing law, the timing law and the Matalon-Packter law. We verify whether our numerical approach of the Cahn-Hilliard formulation presented above can capture these important experimental findings.

A Liesegang band evolution is simulated where the noise effects are absent. The numerical investigation adopts a pseudo-1D solution strategy (1D solution of a single column of quadrilateral elements) for numerical efficiency in mesh refinement studies. The pseudo-1D models were found to deliver identical results to their true 2D counterparts for the scaling law analysis.

The first example demonstrates the capacity of the phase separation model in terms of governing the formation of regular Liesegang stripes and yielding four well-established empirical laws calibrated by laboratory experiments. The domain selected for study is a rectangle with the height L_x and the width L_y as shown in Figure A1a.
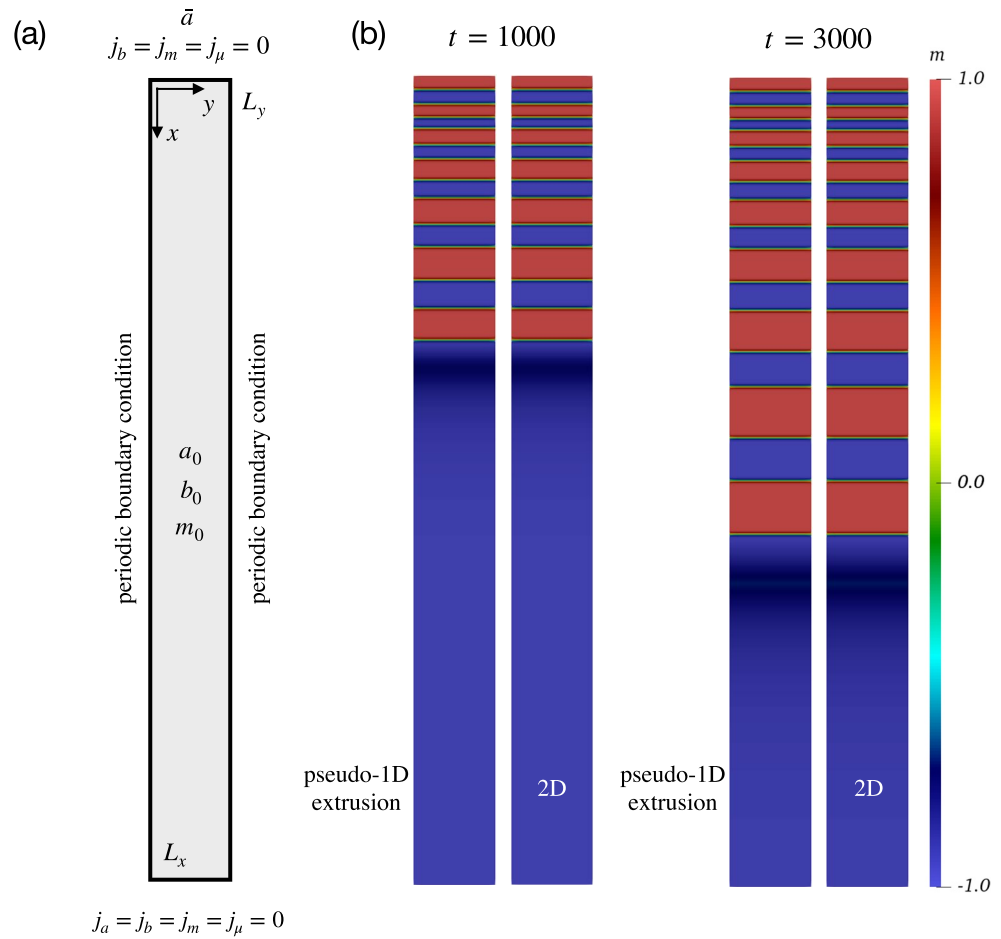
Figure A1. Liesegang striping: (a) Schematic of the numerical setup and (b) comparison of the distribution of m between the pseudo-1D-extrusion and 2D cases at time $t = 1{,}000$ and $t = 3{,}000$. These pseudo-1D results extrude $L_y = 0.125$ to $L_y = 32$ along the y-direction.

For the validation and parameter studies, we simulate both pseudo-1D (a single row of quadrilateral elements) and real 2D domains and compare their results. The domain size for the pseudo-1D and 2D are $L_x = 320 \times L_y = 0.125$ and $L_x = 320 \times L_y = 32$, respectively. Periodic boundary conditions are applied in the y-direction on the vertical boundaries and no-flux boundary conditions $j_a = j_b = j_m = j_\mu = 0$ on the bottom boundary. At the top boundary, we adopt a constant concentration $\bar{a} = 100$ for the reagent A by the Dirichlet boundary condition, with no-flux boundary conditions $j_b = j_m = j_\mu = 0$ for other variables. The initial conditions are $a_0 = 0$, $b_0 = 1.0$, and $m_0 = -1.0$. Regular Liesegang striping patterns are generated by neglecting the noise effect (i.e., η_c vanishes). We use a uniform grid of $2{,}560 \times 1$ for the pseudo-1D problem and $2{,}560 \times 256$ for the 2D problem with a time step of $\Delta t = 2.5 \times 10^{-5}$. Table A1 lists the parameters used.

Table A1
Material Properties for Liesegang Band Simulation

Properties	Values
Diffusion coefficient D_a	1.0
Diffusion coefficient D_b	1.0
Reaction rate κ	1.0
mobility λ	1.0
Parameter ε	1.0
Parameter γ	1.0
Gradient parameter σ	0.2
Noise effect parameter η_c	0

Figure A1 displays the distribution of the normalized product concentration m at time $t = 1,000$ and $t = 3,000$ for the pseudo-1D extrusion to 256 quadrilateral elements as reference 2D scenario. Periodic precipitation bands with increasing width are generated as the reaction-diffusion front propagates, forming regular Liesegang band patterns. The numerical results are reproducing observations from controlled laboratory experiments supporting the argument that an approach based on material balances and first principles is a promising strategy for analysis of the empirical laws (Droz et al., 1999). These results qualitatively match experiments except for one relatively thick stripe at the top edge. There may be a few thick stripes near the top edge. Thus, the discrepancy of the model results at the top boundary is similar to the observations in laboratory experiments (Droz et al., 1999) where at the boundary condition Ostwald ripening effects (Ostwald, 1902) have been argued to overcome the clear definition of thin stripes in the wake of the propagating thicker leading bands (Ammar & Al-Ghoul, 2020).

The results from the pseudo-1D case are in perfect agreement with the extruded 2D case, as shown in Figures A1b and A2a. Therefore, for the sake of computational efficiency, we employ the pseudo-1D domain for parameter studies and Zebra rock sample calibration in Section 2.3 and 2.4. A real 2D scenario is considered for the transition from bands to spots in Section 2.5.
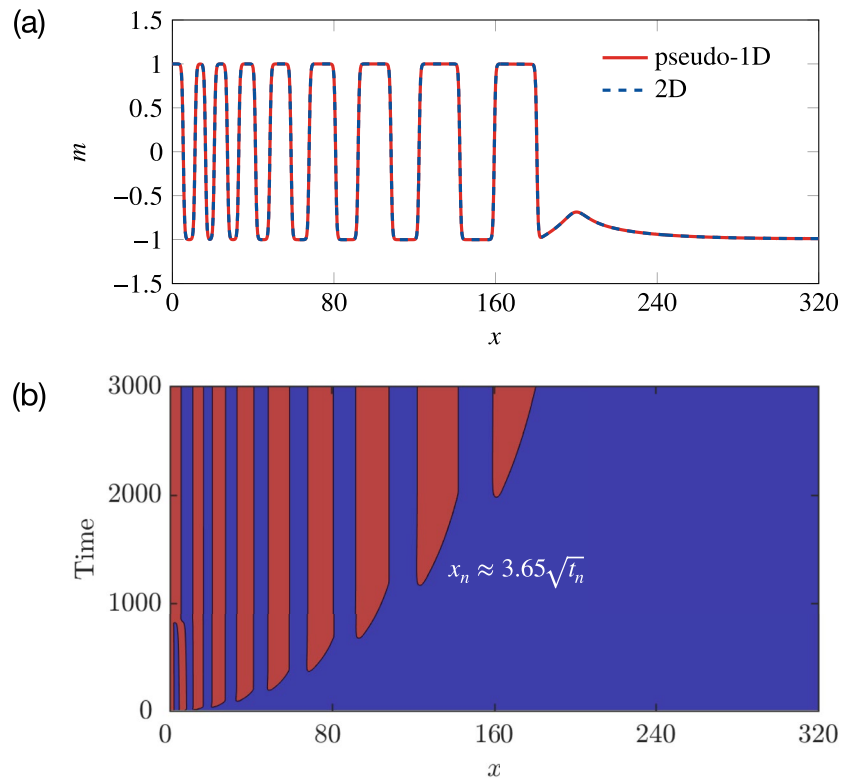
Figure A2. (a) m distributions comparison of the pseudo-1D and 2D simulations at time $t = 3,000$ along x-axis and (b) m spatio-temporal evolution along x-axis.

Next, we quantitatively verify our numerical results by investigating the behaviour of Liesegang striping in terms of timing, spacing, Matalon-Packter, and width laws. Figure A2a displays the thickness of periodic stripes and interband spacing along the x-axis. First, the *timing law* indicates that the diffusion front advances proportionally to the square root of the time $x \propto \sqrt{t}$ (Morse & Pierce, 1903). Our results follow the linear relationship between the position of the nth band and the square root of its appearance time as $x_n \approx 3.65\sqrt{t_n}$, as Figure A2b shows. Next, the *spacing law* relates the location of subsequent stripes by $x_{n+1}/x_n = 1 + p$ where $1 + p$ is the spacing coefficient. The spacing coefficient $1 + p > 0$ denotes the normal Liesegang stripes, whereas $1 + p < 0$ represents the revert Liesegang stripes (Chopard et al., 1994; Karam et al., 2011). In this case, the estimated $1 + p$ is around 1.25, denoting the normal Liesegang stripes as Figure A3a shows. Additionally, the phenomenological *Matalon-Packter law*

$$p = F(b_0) + G(b_0)\frac{b_0}{a_0}$$

associates the parameter p with the initial concentrations of the reagents A and B (Matalon & Packter, 1955). We increase the outer reagent a_0 from 25 to 400 and fit the spacing coefficient by an inverse function as $1 + p = 1.18 + 6.95/a_0$ in Figure A4, demonstrating that our numerical method reproduces the spacing and Matalon-Packter laws. Finally, the *width law* states that the band width w_n is proportional to the position x_n of the band as $x_n \propto w_n$. The linear relationship between x_n and w_n is demonstrated in Figure A3. With all four empirical laws observed in the Liesegang phenomenon being successfully reproduced, the model is properly benchmarked. Interestingly we obtain similar evolution patterns with coarser resolution in space and time when we simulate stripes in 2D. We, however, proceed with the higher accuracy provided by the pseudo-1D simulation for the parameter studies as presented in Section 2.3 and the numerical inversion of Zebra rock patterns in Sections 2.4.
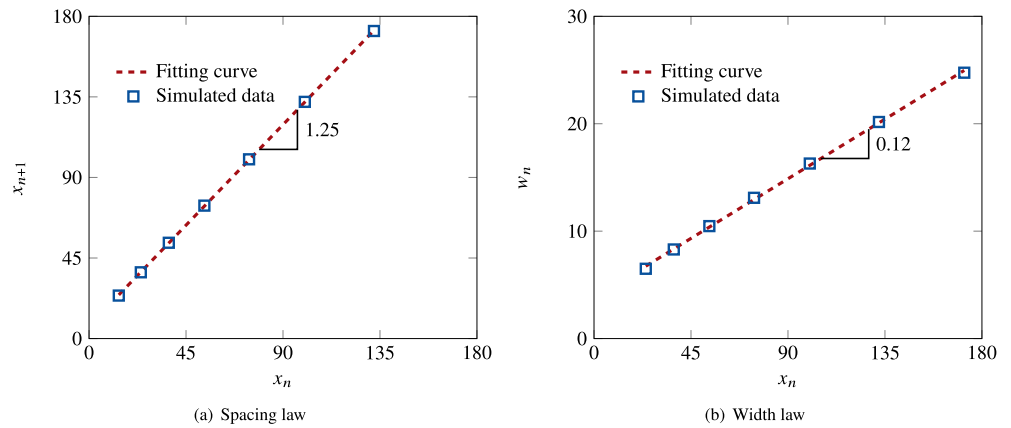
Figure A3. (a) Spacing and (b) width laws verification of Liesegang band.
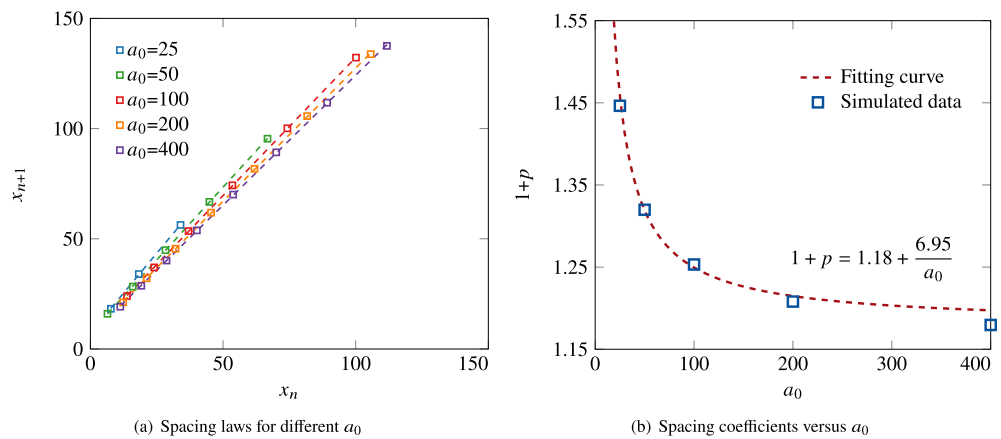

Figure A4. Verification of Matalon-Packter law for Liesegang stripes: (a) spacing laws for different a_0 and (b) spacing coefficient versus a_0.

Data Availability Statement

The Finite Element Method code and simulation data can be downloaded from Mendeley Data via https://data.mendeley.com/v1/datasets/sjjw5ctwfh/draft?a=5222ece1-4366-478c-a451-2c0641af2e29.

References

Abrajevitch, A., Pillans, B. J., Roberts, A. P., & Kodama, K. (2018). Magnetic properties and paleomagnetism of Zebra Rock, Western Australia: Chemical remanence acquisition in hematite pigment and Ediacaran geomagnetic field behavior. *Geochemistry, Geophysics, Geosystems*, *19*(3), 732–748. https://doi.org/10.1002/2017gc007091

Al-Ghoul, M., Ghaddar, T., & Moukalled, T. (2009). Pulse-front propagation and interaction during the growth of CdS nanoparticles in a gel. *The Journal of Physical Chemistry B*, *113*(34), 11594–11603. https://doi.org/10.1021/jp9022647

Al-Ghoul, M., & Sultan, R. (2019). Simulation of geochemical banding: Theoretical modeling and fractal structure in acidization-diffusion-precipitation dynamics. *Physical Review E*, *100*(5), 052214. https://doi.org/10.1103/physreve.100.052214

Ammar, M., & Al-Ghoul, M. (2020). Band propagation, scaling laws, and phase transition in a precipitate system III: Effect of the anions of precursors. *The Journal of Physical Chemistry A*, *124*(1), 39–45. https://doi.org/10.1021/acs.jpca.9b09448

Antal, T., Droz, M., Magnin, J., Pekalski, A., & Rácz, Z. (2001). Formation of Liesegang patterns: Simulations using a kinetic Ising model. *The Journal of Chemical Physics*, *114*(8), 3770–3775. https://doi.org/10.1063/1.1342858

Antal, T., Droz, M., Magnin, J., & Rácz, Z. (1999). Formation of Liesegang patterns: A spinodal decomposition scenario. *Physical Review Letters*, *83*(15), 2880–2883. https://doi.org/10.1103/physrevlett.83.2880

Antal, T., Droz, M., Magnin, J., Rácz, Z., & Zrinyi, M. (1998). Derivation of the Matalon-Packter law for Liesegang patterns. *The Journal of Chemical Physics*, *109*(21), 9479–9486. https://doi.org/10.1063/1.477609

Arguello, M. E., Gumulya, M., Derksen, J., Utikar, R., & Calo, V. M. (2022). Phase-field modeling of planar interface electrodeposition in lithium-metal batteries. *Journal of Energy Storage*, *50*, 104627. https://doi.org/10.1016/j.est.2022.104627

Arguello, M. E., Labanda, N. A., Calo, V. M., Gumulya, M., Utikar, R., & Derksen, J. (2022). Dendrite formation in rechargeable lithium-metal batteries: Phase-field modeling using open-source finite element library. *Journal of Energy Storage*, *53*, 104892. https://doi.org/10.1016/j.est.2022.104892

Arguello, M. E., Labanda, N. A., Calo, V. M., Gumulya, M., Utikar, R., & Derksen, J. (2023). Three-dimensional experimental-scale phase-field modeling of dendrite formation in rechargeable lithium-metal batteries. *Journal of Energy Storage*, *62*, 106854. https://doi.org/10.1016/j.est.2023.106854

Arndt, D., Bangerth, W., Blais, B., Clevenger, T. C., Fehling, M., Grayver, A. V., et al. (2020). The deal.II library, version 9.2. *Journal of Numerical Mathematics*, *28*(3), 131–146. https://doi.org/10.1515/jnma-2020-0043

Behnoudfar, P., Hobbs, B. E., Ord, A., Espath, L., & Calo, V. M. (2022). Localized folding of thick layers. *Journal of Structural Geology*, *161*, 104669. https://doi.org/10.1016/j.jsg.2022.104669

Bertozzi, A. L., Esedoglu, S., & Gillette, A. (2007). Inpainting of binary images using the Cahn–Hilliard equation. *IEEE Transactions on Image Processing*, *16*(1), 285–291. https://doi.org/10.1109/tip.2006.887728

Büki, A., Kárpáti-Smidróczki, É., & Zrínyi, M. (1995). Computer simulation of regular Liesegang structures. *The Journal of Chemical Physics*, *103*(23), 10387–10392. https://doi.org/10.1063/1.469875

Cahn, J. W. (1961). On spinodal decomposition. *Acta Metallurgica*, *9*(9), 795–801. https://doi.org/10.1016/0001-6160(61)90182-1

Cahn, J. W., & Hilliard, J. E. (1958). Free energy of a nonuniform system. I. Interfacial free energy. *The Journal of Chemical Physics*, *28*(2), 258–267. https://doi.org/10.1063/1.1744102

Chopard, B., Luthi, P., & Droz, M. (1994). Reaction-diffusion cellular automata model for the formation of Leisegang patterns. *Physical Review Letters*, *72*(9), 1384–1387. https://doi.org/10.1103/physrevlett.72.1384

Christoph, J., Strasser, P., Eiswirth, M., & Ertl, G. (1999). Remote triggering of waves in an electrochemical system. *Science*, *284*(5412), 291–293. https://doi.org/10.1126/science.284.5412.291

Cier, R., Labanda, N., & Calo, V. (2022). Compaction localization in geomaterials: A mechanically consistent failure criterion. *arXiv preprint arXiv: 2202.03849*. Retreived from https://arxiv.org/abs/2202.03849

Cirillo, E. N. M., Ianiro, N., & Sciarra, G. (2013). Allen–Cahn and Cahn–Hilliard-like equations for dissipative dynamics of saturated porous media. *Journal of the Mechanics and Physics of Solids*, *61*(2), 629–651. https://doi.org/10.1016/j.jmps.2012.08.014

Condie, K. C. (2016). Chapter 8 - The atmosphere and hydrosphere. In *Earth as an evolving planetary system* (3rd ed., pp. 237–278). Academic Press.

Cooper, B. (2012). The incomputable reality. *Nature*, *482*(7386), 465. https://doi.org/10.1038/482465a

Dayeh, M., Ammar, M., & Al-Ghoul, M. (2014). Transition from rings to spots in a precipitation reaction–diffusion system. *RSC Advances*, *4*(104), 60034–60038. https://doi.org/10.1039/c4ra11223g

Deike, R. G. (1990). Dolomite dissolution rates and possible holocene dedolomitization of water-bearing units in the edwards aquifer, south-central Texas. *Journal of Hydrology*, *112*(3–4), 335–373. https://doi.org/10.1016/0022-1694(90)90023-q

DeWitt, S., Rudraraju, S., Montiel, D., Andrews, W. B., & Thornton, K. (2020). PRISMS-PF: A general framework for phase-field modeling with a matrix-free finite element method. *npj Computational Materials*, *6*(1), 1–12. https://doi.org/10.1038/s41524-020-0298-5

Droz, M., Magnin, J., & Zrinyi, M. (1999). Liesegang patterns: Studies on the width law. *The Journal of Chemical Physics*, *110*(19), 9618–9622. https://doi.org/10.1063/1.478927

Fei, F., Choo, J., Liu, C., & White, J. A. (2022). Phase-field modeling of rock fractures with roughness. *International Journal for Numerical and Analytical Methods in Geomechanics*, *46*(5), 841–868. https://doi.org/10.1002/nag.3317

Geidans, L. (1981). *Zebra rock of Western Australia* (Vol. 3(22)).Geological society of Australia.

Gómez, H., Calo, V. M., Bazilevs, Y., & Hughes, T. J. (2008). Isogeometric analysis of the Cahn–Hilliard phase-field model. *Computer Methods in Applied Mechanics and Engineering*, *197*(49), 4333–4352. https://doi.org/10.1016/j.cma.2008.05.003

Hancock, P. (1968). *Location and investigation of zebra rock occurrences, East Kimberley region* Annual Report (pp. 67–68). Geological Survey of Western Australia.

Hantz, P., & Biró, I. (2006). Phase separation in the wake of moving fronts. *Physical Review Letters*, *96*(8), 088305. https://doi.org/10.1103/physrevlett.96.088305

Haskell, R. W. (1973). Introduction to the thermodynamics of spinodal decomposition. *Journal of the American Ceramic Society*, *56*(7), 355–360. https://doi.org/10.1111/j.1151-2916.1973.tb12685.x

Hobbs, B. E., Ord, A., & Regenauer-Lieb, K. (2011). The thermodynamics of deformed metamorphic rocks: A review. *Journal of Structural Geology*, *33*(5), 758–818. https://doi.org/10.1016/j.jsg.2011.01.013

Hobson, R. A. (1930). Zebra rock from the East Kimberley. *Journal of the Royal Society of Western Australia*, *16*, 57–70.

Holba, V., & Fusek, F. (2000). Gravity effect on the formation of periodic precipitation patterns. *Collection of Czechoslovak Chemical Communications*, *65*(9), 1438–1442. https://doi.org/10.1135/cccc20001438

Holland, H. D. (2006). The oxygenation of the atmosphere and oceans. *Philosophical Transactions of the Royal Society B: Biological Sciences*, *361*(1470), 903–915. https://doi.org/10.1098/rstb.2006.1838

Hu, M., Schrank, C., & Regenauer-Lieb, K. (2020). Cross-diffusion waves in hydro-poro-mechanics. *Journal of the Mechanics and Physics of Solids*, *135*, 103632. https://doi.org/10.1016/j.jmps.2019.05.015

Hu, M., Sun, Q., Schrank, C., & Regenauer-Lieb, K. (2022). Cross-scale dynamic interactions in compacting porous media as a trigger to pattern formation. *Geophysical Journal International*, *230*(2), 1280–1291. https://doi.org/10.1093/gji/ggac115

Itatani, M., Fang, Q., & Nabika, H. (2021). Modification of the Matalon–Packter law for self-organized periodic precipitation patterns by incorporating time-dependent diffusion flux. *The Journal of Physical Chemistry B*, *125*(25), 6921–6929. https://doi.org/10.1021/acs.jpcb.1c02175

Karam, T., El-Rassy, H., & Sultan, R. (2011). Mechanism of revert spacing in a $PbCrO_4$ Liesegang system. *The Journal of Physical Chemistry A*, *115*(14), 2994–2998. https://doi.org/10.1021/jp200619g

Kawahara, H., Yoshida, H., Yamamoto, K., Katsuta, N., Nishimoto, S., Umemura, A., & Kuma, R. (2022). Hydrothermal formation of Fe-oxide bands in zebra rocks from northern Western Australia. *Chemical Geology*, *590*, 120699. https://doi.org/10.1016/j.chemgeo.2021.120699

Kelka, U., Veveakis, M., Koehn, D., & Beaudoin, N. (2017). Zebra rocks: Compaction waves create ore deposits. *Scientific Reports*, *7*(1), 1–9. https://doi.org/10.1038/s41598-017-14541-3

Kulkarni, S. D., Takawane, S. D., Walimbe, P. C., Takale, K. D., & Kulkarni, P. S. (2022). Recognition of spatiotemporal patterns of the periodically precipitating 2D reaction-diffusion system by determination of precise band location: Implications on the Matalon-Packter law. *JCIS Open*, *6*, 100053. https://doi.org/10.1016/j.jciso.2022.100053

Larcombe, C. (1924). *Rock specimens from Ord River and Oakover River respectively* Annual Report (Vol. 19). Geological Survey of Western Australia.

Larcombe, C. (1926). *Some rocks from four miles east of Argyle Station, Ord River, King district, Kimberley division* Annual Report (Vol. 23). Geological Survey of Western Australia.

L'Heureux, I. (2013). Self-organized rhythmic patterns in geochemical systems. *Philosophical Transactions of the Royal Society A: Mathematical, Physical & Engineering Sciences*, *371*(2004), 20120356. https://doi.org/10.1098/rsta.2012.0356

Li, S., Dutta, B., Cannon, S., Daymude, J. J., Avinery, R., Aydin, E., et al. (2021). Programming active cohesive granular matter with mechanically induced phase changes. *Science Advances*, *7*(17), eabe8494. https://doi.org/10.1126/sciadv.abe8494

Liesegang, R. E. (1906). Eine scheinbar chemische Fernwirkung. *Annalen der Physik*, *324*(2), 395–406. https://doi.org/10.1002/andp.19063240210

Liu, C., Hu, M., & Regenauer-Lieb, K. (2022). Liesegang patterns interpreted as a chemo-hydromechanical instability. In *Multiscale processes of instability, deformation and fracturing in geomaterials: Proceedings of 12th international workshop on bifurcation and degradation in geomechanics* (pp. 59–66).

Loughnan, F., & Roberts, F. (1990). Composition and origin of the 'zebra rock' from the East Kimberley region of Western Australia. *Australian Journal of Earth Sciences*, *37*(2), 201–205. https://doi.org/10.1080/08120099008727920

Mansour, A. A., & Al-Ghoul, M. (2015). Band propagation, scaling laws, and phase transition in a precipitate system. 2. Computational study. *The Journal of Physical Chemistry A*, *119*(35), 9201–9209. https://doi.org/10.1021/acs.jpca.5b05069

Matalon, R., & Packter, A. (1955). The Liesegang phenomenon. I. Sol protection and diffusion. *Journal of Colloid Science*, *10*(1), 46–62. https://doi.org/10.1016/0095-8522(55)90076-3

Mattievich, E., Chadwick, J., Cashion, J. D., Boas, J. F., Clark, M., & Mackie, R. (2003). Macroscopic ferronematic liquid crystals determine the structure of Kimberley Zebra Rock. In *27th ann. cond. matt. phys. meet. conf. handb.*

May, S. M., Hoffmeister, D., Wolf, D., & Bubenzer, O. (2019). Zebra stripes in the Atacama Desert revisited–Granular fingering as a mechanism for zebra stripe formation? *Geomorphology*, *344*, 46–59. https://doi.org/10.1016/j.geomorph.2019.07.014

Morse, H. W., & Pierce, G. W. (1903). Diffusion and supersaturation in gelatine. 129. *Physical Review*, *17*(3), 129–150. https://doi.org/10.1103/physrevseriesi.17.129

Msharrafieh, M., Al-Ghoul, M., Zaknoun, F., El-Rassy, H., El-Joubeily, S., & Sultan, R. (2016). Simulation of geochemical banding I: Acidization-precipitation experiments in a ferruginous limestone rock. *Chemical Geology*, *440*, 42–49. https://doi.org/10.1016/j.chemgeo.2016.06.028

Nabika, H., Itatani, M., & Lagzi, I. (2019). Pattern formation in precipitation reactions: The Liesegang phenomenon. *Langmuir*, *36*(2), 481–497. https://doi.org/10.1021/acs.langmuir.9b03018

Nakouzi, E., & Sultan, R. (2011). Fractal structures in two-metal electrodeposition systems I: Pb and Zn. *Chaos: An Interdisciplinary Journal of Nonlinear Science*, *21*(4), 043133. https://doi.org/10.1063/1.3664343

Ostwald, W. (1902). *Lehrbuch der allgemeinen Chemie* (Vol. 2). W. Engelmann.

Regenauer-Lieb, K., Hu, M., Schrank, C., Chen, X., Clavijo, S. P., Kelka, U., et al. (2021). Cross-diffusion waves resulting from multiscale, multi-physics instabilities: Theory. *Solid Earth*, *12*(4), 869–883. https://doi.org/10.5194/se-12-869-2021

Retallack, G. (2021). Zebra rock and other Ediacaran paleosols from Western Australia. *Australian Journal of Earth Sciences*, *68*(4), 532–556. https://doi.org/10.1080/08120099.2020.1820574

Sultan, R., Ortoleva, P., DePasquale, F., & Tartaglia, P. (1990). Bifurcation of the Ostwald-Liesegang supersaturation-nucleation-depletion cycle. *Earth-Science Reviews*, *29*(1–4), 163–173. https://doi.org/10.1016/0012-8252(0)90034-s

Sun, Q., Hu, M., & Regenauer-Lieb, K. (2022). Cross-scale dynamic interactions in compacting porous geomaterials as a trigger to instabilities. In *Multiscale processes of instability, deformation and fracturing in geomaterials: Proceedings of 12th international workshop on bifurcation and degradation in geomechanics* (pp. 67–73).

Theljani, A., Houichet, H., & Mohamed, A. (2020). An adaptive Cahn-Hilliard equation for enhanced edges in binary image inpainting. *Journal of Algorithms & Computational Technology*, *14*, 1748302620941430. https://doi.org/10.1177/1748302620941430

Thomas, S., Lagzi, I., Molnár, F., Jr., & Rácz, Z. (2013). Probability of the emergence of helical precipitation patterns in the wake of reaction-diffusion fronts. *Physical Review Letters*, *110*(7), 078303. https://doi.org/10.1103/physrevlett.110.078303

Vignal, P., Collier, N., Dalcin, L., Brown, D., & Calo, V. (2017). An energy-stable time-integrator for phase-field models. *Computer Methods in Applied Mechanics and Engineering*, *316*, 1179–1214. https://doi.org/10.1016/j.cma.2016.12.017

Wang, Y., Chan, M. A., & Merino, E. (2015). Self-organized iron-oxide cementation geometry as an indicator of paleo-flows. *Scientific Reports*, *5*(1), 1–15. https://doi.org/10.1038/srep10792

Yoshida, H., Katsuta, N., Sirono, S.-i., Nishimoto, S., Kawahara, H., & Metcalfe, R. (2020). Concentric Fe-oxyhydroxide bands in dacite cobbles: Rates of buffering chemical reactions. *Chemical Geology*, *552*, 119786. https://doi.org/10.1016/j.chemgeo.2020.119786